Environmental and internal controls on Lagrangian transitions from closed cell mesoscale cellular convection over subtropical oceans

Ryan Eastman, Isabel L. McCoy, Robert Wood

University of Washington, Atmospheric Sciences

Corresponding Author Information:

Ryan Eastman

University of Washington Department of Atmospheric Sciences

Box 351640, Seattle WA 98195

Email: rmeast@atmos.washington.edu

Abstract

Classifications of mesoscale cellular convection (MCC) for warm clouds in the marine boundary layer are produced using a human-trained machine-learning algorithm applied to MODIS daytime liquid water path data. The classifier distinguishes closed, open, and disorganized cellular MCC. This work uses a set of trajectories in four eastern subtropical ocean basins to compare meteorological variables and the structures of cloudy boundary layers for trajectories that all begin as closed cells, but evolve either into open cells, disorganized cells, or remain closed cells over one afternoon-afternoon diurnal cycle.

Results show strong contrasts between the three trajectory sets: Trajectories for MCC that remain closed cell are more frequently observed upwind, nearer coasts, while trajectories that break into open and disorganized cells begin farther downwind. The frequency at which closed cells transition to open cells is seasonally invariant. The fraction of trajectories that stay closed MCC varies throughout the year in opposition to those that break into disorganized cells. Trajectories remain closed cell more frequently in spring and summer when the trade inversion is stronger.

The closed-disorganized MCC transition is associated with weaker subsidence, a weaker inversion, a drier overlying free troposphere, and enhanced nighttime boundary layer deepening, suggesting a warming-drying mechanism for cloud breakup. The closed-open transition occurs in meteorological conditions more similar to closed-closed trajectories. However, prior to the transition, the closed-open trajectories exhibit stronger surface winds, lower cloud droplet number concentrations, and rain more heavily overnight. Conclusions suggest that multiple, independent mechanisms drive changes in cloud amount and morphology.

Introduction & Motivation

Low-altitude, optically thick marine clouds cool Earth's oceans by reflecting sunlight and emitting infrared radiation to space (Hartmann et al. 1992, L'Ecuyer et al. 2019). Marine low clouds cover nearly 200 million square kilometers of ocean on average during the day (Hahn & Warren, 2007), while overcast marine cloud scenes are estimated to reflect 30-40% (Bender et al. 2016) of incoming solar radiation. Taken together, the extent and albedo of marine clouds has an effect equivalent to covering 60-80 million square kilometers of dark ocean with perfect reflectors. Modifications to marine cloud brightness and cover can therefor have significant consequences for climate.

Attempts to understand the mechanics of marine cloud cover evolution have been made using a variety of approaches: Comparing long-term climatologies (yearly, seasonal, monthly) of cloud cover and environmental predictor variables shows correlations between variables (for example: Norris, 1998), though no single variable predicts a majority of cloud variability (Klein, 1997), confounding relationships between variables are difficult to disentangle, and causality cannot be attributed to predictors without a time dimension (Qu et al. 2015; Klein, 2017). In-situ studies using aircraft or ships can collect a large amount of data at a very high resolution, but they lack the longevity needed to build up statistical significance and also typically lack the spatial extent needed to follow cloud scenes as they respond to their environment while advecting downstream. Studies using computer models capable of resolving circulations on the sub-cloud level can isolate predictors and assess causality, but are computationally expensive and exist at the mercy of parameterized model physics (Guichard & Couvreux, 2017). Here we use a newer Lagrangian approach (introduced in Eastman & Wood 2016): Following thousands of cloudy parcels as they evolve in time and space while sampling cloud properties and environmental drivers on a sub-daily timescale using polar-orbiting satellites and reanalysis grids. This approach provides sample sizes large enough to attain statistical significance and control for confounding behaviors, while also assessing causality with the introduction of a time dimension.

This work is concerned with the Lagrangian evolution of the cellular organization of stratiform clouds over the subtropical oceans (Agee 1987). In marine environments characterized by a strong temperature and humidity inversion (as is often observed in the eastern subtropical oceans), a cool and moist boundary layer is typically observed under a warm and dry free-troposphere. Here Stratocumulus (Sc) clouds tend to organize into broad, overcast, optically thick closed cells, sustained by overturning driven by radiative cooling at cloud top (Wood 2012). Occasionally closed cells break into open cells which are characterized by relatively narrow bands of optically thick clouds flanked by optically thin 'veil clouds' (Wood et al. 2018) with broad clear regions between the cloudy edges (Wood et al. 2008). As they advect equatorward and westward in the trade winds, subtropical closed and open cells eventually evolve into more disorganized structures (Muhlbauer et al., 2014) with widely-spaced and somewhat randomly distributed cloudy cores surrounded by thin veil clouds and fields of shallow cumulus.

The drivers of transitions from closed to open cells versus closed to disorganized cells are the focus of this work. Prior research suggests that open cell formation from existing closed cells is triggered by precipitation processes (Wang and Feingold, 2009). Savic-Jovcic & Stevens

(2008) use a Large Eddy Simulation to show how cool and moist perterbations in near-surface airmasses formed by evaporation of rain drops (cold pools) can shape and propagate convective elements in drizzling Sc. Terai & Wood (2013) state that cold pool processes do exert thermodynamic and dynamic forces on the PBL, but stop short of showing that they are responsible for any changes in cellular organization. Precipitation was tested as a possible driver of subtropical Sc breakup in Eastman and Wood (2016), but was found to be of little importance compared to the depth of the boundary layer, which covaries positively with rain rate. That work did not account for specific transitions in cellular organization, but it suggests that, in many cases, the breakup of Sc is not driven by precipitation. Instead, processes that warm and deepen the boundary layer are more important for Sc breakup. Now that we can specifically test drivers of changes in cellular organization, which may be significantly different from one another, we may find that the conflicting conclusions about the role of rain in Sc breakup are not as disparate as previously thought.

The cellular structure of marine clouds has an effect on albedo in a few ways: Closed cells are typically cloudier than open, which are in-turn cloudier than disorganized cells. Further complicating the picture, closed cells have been shown to have a higher albedo for an equivalent cloud amount versus open and disorganized cells (McCoy et al. 2017), indicating that cloud condensate and microphysical properties are also likely important for setting scene albedo, in addition to cloud cover. This necessitates further study of these organizational structures in order to understand what meteorological conditions and internal processes may be driving transitions in cellular organization. Climate models that use parameterizations based on meteorology to simulate cloud properties will be improved if they can better simulate cloud cellular properties and the conditions associated with them.

Cellular structures in clouds can now be detected and defined using high-resolution satellite imagery and efficient machine-learning techniques (Wood & Hartmann 2006, Stevens et al. 2020, Yuan et al. 2020). These products can be combined with our aforementioned Lagrangian analysis to sample cellular structures repeatedly for the same cloud scenes as they advect in the subtropical trade winds. Using these techniques, we will study the meteorology and internal cloud processes driving MCC evolution in subtropical marine low clouds.

Data Sources

This work will combine several data sources from polar orbiting satellites and model reanalysis fields. Satellite data come from several platforms orbiting in NASA's Afternoon-Train (A-Train) constellation, including: The Moderate Resolution Imaging Spectroradiometer (MODIS) and the Advanced Microwave Scanning Radiometer for EOS (AMSR-E) both orbiting aboard the Aqua satellite, the Cloud-Aerosol Lidar and Infrared Pathfinder Satellite Observation (CALIPSO), and the spaceborne cloud profiling radar aboard CloudSat. The A-Train satellites orbit together with equator crossing times at 1:30 and 13:30 local times, allowing for near-simultaneous sampling of atmospheric features by several different instruments. Meteorological data come from two reanalysis datasets: Primarily the European Centre for Medium-Range Weather Forecasts (ECMWF) ERA-Interim reanalysis (Dee et al. 2011) along with the newer ERA5 reanalysis (Copernicus Climate Change Service, 2017), applied here in the

production of rain rate estimates. Reanalysis data fields are interpolated to match the observation times of the A-Train satellites in order to eliminate diurnal sampling biases.

Study regions are chosen in four eastern subtropical ocean basins with similar climatologies, chosen to capture Sc maxima near the west coasts of major continents and also the declining cloud-cover gradients further offshore as the Sc transition into trade Cumulus (Cu). These regions are identical to those in Eastman & Wood (2016, their Figure 1), and are named: the Northeast Pacific, Southeast Pacific, Southeast Atlantic, and the East Indian regions.

Trajectories used here are generated from isobaric ERA-Interim wind fields at 925 hPa using the routine introduced in Bretherton et al. (2010). Trajectories are initiated along the CloudSat/CALIPSO curtain, spaced 200 km apart in the four study regions. Trajectories are run forward for 54 hours. Samples of cloud and meteorological data are taken concurrent with each A-Train flyover at 0, 12, 24, 36, and 48 Trajectory hours, and include all data within a 100km radius of each observation point.

Cloud cover data retrieved along trajectories for day and night come from the mean cloud fraction values in the MODIS cloud mask dataset (Hubanks et al. 2008; Oreopoulos 2005). These are available twice daily on the L3 1°x1° latitude/longitude grid. The MODIS swath is over 2000 km wide, requiring sensor viewing angles over 60° from nadir at the swath edge. Geometric issues arise when clouds are viewed from this oblique angle, causing a high bias in cloud amount at swath edge (Maddux et al. 2010). This Lagrangian project uses MODIS retrievals taken at a variety of viewing angles, so this zenith angle bias is accounted for by subtracting the mean excess in cloud cover from each sample caused by that sample's view angle (Eastman & Wood, 2016). Day and night cloud liquid water path (LWP) comes from the AMSR/E sensor (Wentz & Meissner, 2004) averaged to the 1°x1° L3 grid. AMSR/E provides total LWP, which includes clear and cloudy portions, so total LWP is divided by MODIS cloud fraction to estimate the LWP for cloudy portions only (CLWP).

Cloud droplet number concentration (N_d) estimates come from three sources: Our primary N_d dataset uses a combination of cloud droplet effective radius and liquid water path detected by the MODIS collection 6 daytime-only optical properties dataset (King et al. 2003) and the relationship developed by Boers et al. (2006) and Bennartz (2007) and shown as Equation 1 in Possner et al. (2020). Two other N_d products are compared in Appendix 1: One was developed by Grosvenor & Wood (2018), which uses the collection 5 MODIS optical properties data and a different set of relationships. A third, independent, N_d data source is the Modern-Era Retrospective Analysis for Research and Applications, Version 2 (MERRA-2, Galero et al. (2017), which provides estimates of aerosol concentrations for a variety of different aerosol types and sizes. These concentrations can be combined with the regression coefficients determined in McCoy et al. (2017) to estimate N_d. Due to the difficult-to-retrieve nature of N_d and the possibilities of biases in the data associated with cloud edge retrievals, multiple N_d products are compared here in order to substantiate results.

Day and night rain rate estimates come from the routine introduced in Eastman et al. (2019), which uses the relationship between brightness temperature (T_b) observed by AMSR/E at 89 GHz and rain rate as measured by the rain-profile (Mitrescu et al. 2010; Lebsock and L'Ecuyer 2011) dataset from the CloudSat cloud profiling radar. Rain rate estimation relies on the positive relationship between T_b and rain rate (Miller and Yuter, 2013), where warm T_b is associated with greater in-cloud LWP and heavier rain rates. The product is able to produce

estimates of rain rate after controlling for three other variables that also drive T_b variation: surface wind speed, column water vapor, and sea surface temperature. Column water vapor is measured by the AMSR/E (Wentz and Meissner, 2004). For the updated version of this precipitation dataset, SST and wind speed now come from the ERA5 reanalysis. Rain rates are resolved in 4x6 km grid boxes, which is of a sufficient resolution to see most individual cellular elements in Sc cloud decks.

The depth of the planetary boundary layer (PBL), assumed to be the same as the height of the trade inversion, is estimated using the difference between cloud top temperature and SST for a subset of clouds assumed to sit at the trade inversion. The depth of this layer is determined using a parameterized lapse rate from Wood and Bretherton (2004). The temperature of the clouds at inversion top is estimated using the algorithm developed in Eastman et al. (2016 & 2018) which is tuned through a comparison between MODIS cloud top temperature histograms and CALIPSO vertical feature mask data (Vaughan et al. 2004).

The cellular organization of marine cloud cover is determined using a human-trained neural network developed in Wood and Hartmann (2006) and applied in McCoy et al. (2017) and Muhlbauer et al. (2014). This algorithm is applied to the MODIS collection 6 daytime-only LWP field from 2003-2011 to determine the type of low cloud dominating a 256x256 km scene. In this updated dataset, clouds are classified into three mesoscale cellular convection (MCC) types: closed cells, open cells, and disorganized cells. The original fourth classification category of homogeneous/no organization has been collapsed into closed cells due to its limited occurrence, as in McCoy et al. (2017). Centers of classified scenes are spaced 128 km apart, producing some overlap between each classified box, but increasing the amount of data within each box to improve the classification. An example of the classifier is shown in Figure 1, where classifier output is overlaid on a MODIS Aqua daytime cloud scene. Numbers represent MCC classifications, where 0 is open cells, 1 is closed cells, and 3 is disorganized. Scenes that may contain overlying cold clouds are filtered out of the analysis by comparing cloud top temperature to SST and removing scenes with a maximum difference greater than 30C.

In order to determine an MCC classification for scenes tracked in our Lagrangian system, a frequency distribution of all MCC box centers within 200km of each sampling point is produced at each point. If any classification is greater than 50% represented in that distribution, the scene is considered to be that MCC type. Examples of this approach are shown graphically in Figure 2. This analysis was repeated using two other approaches for classifying scenes, producing qualitatively identical results: One approach assigned the single MCC classification nearest to the trajectory sample as the MCC type for that sample, while the other assigned the sample MCC type to the majority MCC type in the frequency distribution, not requiring 50% or greater representation.

This study also relies on several meteorological variables from reanalysis fields. Surface wind speed, subsidence at 700 hPa (ω_{700}), sea surface temperature (SST), lower tropospheric stability (LTS, θ_{700}-θ_{1000}), and humidity at 700 hPa (q_{700}) come from the ERA-Interim dataset.

Methods and Results

a) Climatological behavior of transitions

Here, we focus on 24-hour (13:30-13:30) Lagrangian transitions in MCC classifications, specifically looking at trajectories that begin as closed cell Sc. Trajectories are composited into three sets based on their 0-hour and 24-hour MCC classifications: Closed-closed, closed-open, and closed-disorganized. Requiring our trajectories to all begin as closed cells allows for a greater "apples-to-apples" comparison since retrieved cloud variables at 0-hours may otherwise be artificially affected by different cellular structures. The afternoon-afternoon time period is constrained by the MCC data, which are only collected during the daytime overpass of the Aqua satellite. Given this constraint, the compositing of non-matching diurnal cycles cannot produce biases in our results. Nighttime data are collected at the 12-hour observation time for all available data sources. Our 54-hour trajectories are divided into independent, 24-hour afternoon-afternoon subsets in order to maximize the number of 24-hour transitions available to study.

A geographic comparison between our trajectory sets is shown in Figure 3, where trajectories are composited by transition type within each region. The NE Pacific, SE Pacific, and SE Atlantic show similar results, with closed-closed trajectories seen further upwind, in regions with a stronger inversion, than the more comparably located closed-open and closed-disorganized transitions, which tend to occur farther offshore. In the East Indian region the closed-open trajectories tend to occur farther upwind, with the closed-disorganized and closed-closed changes occurring farther offshore, respectively.

The seasonality of closed cell transitions is explored in Figures 4 and 5. Figure 4 shows the fraction of trajectories that begin as closed cells within a 100-day sampling window. A significant seasonal cycle is apparent in every region, with peaks in the early spring for the southern hemisphere regions, but in the early summer for the NE Pacific.

In Figure 5 the fraction of closed cells that break into open (red), break into disorganized (black), or stay closed (blue) are compared between regions. Trajectories remain closed more often when closed cell trajectory starts are more common (from Figure 4). The fraction of closed cells that break into open cells is relatively stable throughout the year. In contrast, the fraction of closed cells that transition to disorganized is seasonally variable, corresponding with the opposing seasonality in the fraction of closed cells that remain closed. The lack of a seasonal cycle in the relative frequency of closed-open transitions is peculiar, given the strong seasonal cycles in most meteorological variables in these regions (Eastman et al. 2017, Their figure 7) and may suggest that the closed-open transition has less sensitivity to seasonally varying meteorology. This contrasts with the relative frequency of the closed-disorganized transition, which exhibits a stronger seasonal cycle, so may likely be driven by varying meteorology. For example, LTS tends to be higher when closed-closed trajectories are most frequently observed in the NE Pacific, SE Pacific, and SE Atlantic (again from Eastman et al. 2017, their figure 7).

b) Composite analysis of cloud and predictor variables

Figures 6 and 7 show regional breakdowns of composited cloud and meteorological variables taken at 0, 12, and 24 hours for our three trajectory sets. Composites represent averages of all trajectories exhibiting that transition type with the transition type specified by color. The vertical extent of the plots represents the 2-sigma standard error, in order to

compare means. Cloud variables compared in Figure 6 show that cloud cover (6a, 6f, 6k, 6p) evolves similarly in each region, but differently for each set: Closed-closed trajectories stay overcast, closed-open trajectories experience some cloud reduction, and closed-disorganized trajectories experience the most cloud loss. The sets remain overcast at the 1:30 sampling time, indicating that the breakup into open and disorganized cells occurs between 1:30 and 13:30. This timing is consistent with the conclusions from the analysis of a much more limited set of closed-to-open cell MCC transition cases in Wood et al. (2008, JGR, Fig. 10), which showed transitions peaking from 3-6 am local time. For our other cloud variables, the NE Pacific, SE Pacific, and SE Atlantic show similar behavior. In those three regions closed-closed trajectories begin and end with the most N_d and the lightest rain rates, and begin with less CLWP and in shallower PBLs. Closed-open trajectories have significantly fewer N_d, greater overnight rain rates, and more CLWP. Closed-disorganized trajectories begin in deeper PBLs, have less overnight CLWP, and lower rain rates, with N_d in-between the other two sets. The E Indian ocean appears to be an outlier in Figure 6, with less distinction between sets. The most significant difference between sets in the E Indian is the stronger rain rate seen throughout the evolution of the closed-open trajectories, agreeing with the rain behavior in the other regions.

Figure 7 shows composites of meteorological variables in the same manner as Figure 6. In all regions except the SE Pacific, q_{700} is lowest for the closed-disorganized set. Wind speed is significantly higher for the closed-open set in all four regions. The sea surface is coolest and LTS is highest for the closed-closed sets in all four regions. Subsidence is lowest at 0 and 12 hours for the closed-disorganized sets in the SE Pacific, SE Atlantic, and NE Pacific.

To further verify results, here we remove the effects of mean geographical and seasonal differences between the trajectory sets using anomalies. Figures 8 and 9 show anomalies combined for all regions for cloud and meteorological variables, respectively. Composites are constructed using deseasonalized anomalies of all variables, with the diurnal cycles also removed. This is necessary when combining numerous trajectories from the different regions, since the regions have differing climatologies and the mean locations of the different transitions are associated with different mean climatologies. Results using anomalies reinforce the results from Figures 6 and 7 with stark contrasts present between the trajectory sets. Closed-open trajectories are associated with significantly stronger winds, reduced N_d, and heavier overnight rain. Closed-disorganized transitions are associated with reduced subsidence and LTS, a drier free troposphere, and warmer sea surface. This suggests that drivers of closed-open cell transitions are distinct from closed-disorganized transitions: Closed-open transitions are associated with internal microphysical and precipitation processes along with stronger winds, while closed-disorganized transitions are driven by surrounding meteorology.

Typically, subtropical Sc PBLs deepen at night due to the increased turbulence and entrainment driven by radiational cooling at cloud top. However, Figure 8d illustrates shallower PBL depth anomalies at night for closed-closed and closed-open trajectories, compared with closed-disorganized. Further, Figures 6d, 6i, 6n, and 6s show closed-closed and closed-open sets have less change in PBL depth over 24 hours compared to closed-disorganized sets. This difference in cycles is likely due to differences in q_{700}, subsidence, and inversion strength seen between the trajectory sets in Figure 9. Taken together, these differences in meteorology for the closed-disorganized set drive: Increased cloud top cooling through a drier free troposphere, stronger entrainment across a weaker inversion, and more PBL deepening given the weaker

compensating downward motion in the troposphere. All of these processes suggest that the clouds are experiencing warming and drying through entrainment of free tropospheric air. In the closed-open transition, the diurnal cycle in precipitation and LWP are enhanced in contrast to the PBL deepening shown in the closed-disorganized cases, suggesting that overnight precipitation processes may drive the cloud evolution instead of drying through PBL deepening and entrainment. These results are summarized in Table 1, which shows which cloud and meteorological variables are most strongly associated with our MCC transitions.

c) Untangling rain and N_d

Rain rate and N_d tend to strongly covary. When rain is present, cloud drops tend to be large and drop concentrations tend to be low. Additionally, the routines and source data used to estimate N_d from satellite observations may introduce biases due to the application of a single routine to several distinct cloud morphologies (Fu et al. 2019). Here, we attempt to untangle these issues by first comparing three different N_d products in our compositing routine. Then, we further subset trajectories into groups where either precipitation or N_d is held somewhat constant while the other variable is unconstrained, allowing for the effects of one to be tested while the other is controlled.

In Figure 10, the N_d analysis from Figure 6, (frames b, g, l, q) is repeated for all regions combined using our default N_d (frame a), using the N_d from Grosvenor and Wood (2018, hereafter: Grosvenor N_d, frame b), and for an entirely independent data source, the N_d derived from MERRA aerosol reanalysis using the regression established by McCoy et al. (2017) (frame c). The separation of groups in all three frames of Figure 10 supports our result, showing that closed-open transitions are associated with fewer N_d at the outset and closed-closed trajectories have the highest N_d. The Grosvenor N_d shows an increasing tendency for the closed-disorganized set, which is at odds with the other two products. This is likely due to the increasingly broken clouds over time in the closed-disorganized transition. The Grosvenor N_d is calculated for clouds that are primarily overcast, so the subset of observations we show that are disorganized and also mostly overcast here represents a very small, and somewhat peculiar slice of our data. A closer look shows that there are 838 closed-disorganized transitions sampled for the Grosvenor N_d, while the other two products have over 4800. This makes the Grosvenor N_d less robust for this set and is likely why the slope is in disagreement with the other products.

In Figure 11 we attempt to untangle the covarying effects of rain and N_d. Here, our trajectory sets are separated by whether trajectories begin with below/above-median precipitation probability or below/above-median N_d. Composites for the covarying variable from our three trajectory sets (closed-closed, closed-open, closed-disorganized) are compared to see whether their behavior is different when their covarying variable is constrained. Results from 11a and 11b show that reduced 0-hour N_d is associated with the closed-open transition regardless of whether rain is likely occurring at 0 hours. This was repeated for overnight (12-hour) rain observations and results were qualitatively identical, indicating that N_d may influence the closed-open transition independently of rain. Frames 11c and 11d show that rainfall appears significantly associated with the closed-open transition regardless of whether N_d is high or low, indicating, like above, that rain may influence the closed-open transition independently

of N_d. These results suggest that rain and N_d may be associated with separate mechanisms driving the closed-open transition, or they may be a symptom of another mechanism that drives the transition while also modifying both N_d and rain rate.

Discussion

Results here are limited to the large-scale meteorological and cloud deck conditions associated with cloud transitions. We have identified three of our tested variables as being associated with closed-open transitions, either prior to the transition in the case of reduced N_d and stronger wind speed, or concurrent with the overnight transition in the case of heavier rain. These results can aid in predicting the likelihood of closed-open transitions or in establishing more realistic boundary conditions in models that study the transition, but they do not directly reveal an exact mechanism for the closed-open transition. The overnight PBL deepening and entrainment drying hypothesis for the closed-disorganized transitions appears well-supported by the data. A corresponding mechanism for the closed-open transition is less clear, but is likely associated with the high overnight LWP and rain rates, perhaps aided by increased wind speed and/or low N_d.

Future work may focus specifically on the closed-open transition, which appears to occur in similar boundary layers with similar meteorology to the unchanged closed-closed trajectories, but with stronger surface winds and different microphysics and rainfall characteristics. Some questions motivated by our results include: Whether wind speed is a driver of the closed-open transition, or whether wind has a strong effect on microphysics or precipitation, and what drives the higher LWP and reduced Nd that tends to precede closed-open transitions? Prior observational work in pristine marine Cu appears to show that stronger wind is associated with more cloud drops (Colón-Robles et al. 2006). Kazil et al. (2016) modelled non-precipitating Sc for a variety of wind speeds and show a stronger LWP diurnal cycle, and higher LWP on average when wind is stronger. This is due to enhanced production of turbulent kinetic energy (TKE) in buoyant updrafts, which could be part of the mechanism driving the closed-open transition. A higher latent heat flux associated with stronger winds would lead to greater condensation and stronger buoyant production of TKE (as explained in Bretherton and Wyant 1997). Scott et al. (2020) go on to show that stronger winds in subtropical Sc regions are associated with enhanced cloud amount, but decreasing optical thickness, which *could* hint at changes in cellular structure. The positive connection between surface wind speed and open cells was mentioned in Wood et al. (2008), however a detailed analysis is lacking. It is possible that other characteristics associated with stronger winds are mechanically responsible for the transition: convergence/divergence, shear within the PBL or across the inversion, additional turbulence within the PBL, or enhanced surface fluxes. Future work concerning the closed-open transition could look back longer than 24-hours to see whether microphysical anomalies are organized around perturbations in the flow, or whether flow perturbations could be influenced by precipitation or microphysical processes in the clouds.

The analysis in section c of our results begins to untangle rain and N_d, suggesting that heavy rain and reduced N_d are independently associated with trajectories that transition from closed-open MCC. A limitation of this analysis is that we only observe precipitation at one moment overnight. Rainfall may be present before or after this observation, making it possible

that all transitions are associated with rain, but not all of the rain is observed. Modelling studies or higher-resolution in-situ studies could aid in determining whether separate mechanisms exist for the closed-open transition, or whether a single mechanism explains the differences in rain, N_d and wind speed.

The geographic limitation of this study raises questions as to whether the nature of the transitions seen in the subtropical Eastern ocean regions is common to other regions. Future work should study transitions in MCC in a range of climatological regions, which may better elucidate a set of mechanisms associated with transitions. Transitions in remote mid-latitude oceans may be free of N_d-altering pollution near the coasts and may also occur where wind speeds are more variable, offering a wider sampling of wind conditions and perhaps better constraints on N_d.

In Eastman & Wood (2016) it was shown that rainfall had little effect on Lagrangian changes in Sc cloud amount. Now that cellular structure can be assessed alongside cloud amount, that result can be clarified: Rainfall does appear associated with the Lagrangian closed-open cell transition, but less-so for the closed-disorganized transition. The closed-disorganized MCC transition is over twice as common as the closed-open transition, and is associated with a greater decline in cloud amount. Therefore, it is likely that the closed-disorganized signal obscured the weaker, less frequent closed-open signal in that work. The new results presented here show that it is imperative that cloud cellular structure be assessed alongside cloud amount if the goal is to properly capture cloud processes.

Conclusions

Mesoscale cellular convection is classified into three groups using a machine learning algorithm: Closed cell, open cell, and disorganized but cellular. Classifications of MCC type are sampled along 24-hour trajectory segments, beginning and ending at 13:30, and sampled every 12 hours by A-Train satellites and ERA-Interim reanalysis fields. Three trajectory sets are analyzed, all of which begin as closed cells and either stay closed, transition into open cells, or transition into disorganized cells.

A geographical comparison of the mean locations of transition types in our four subtropical ocean study regions shows similar mean behaviors in the NE Pacific, SE Pacific, and SE Atlantic regions. In those three regions closed-closed trajectories tend to exist closer to the coasts where LTS is climatologically greater, while closed-open and closed-disorganized transitions occur farther offshore. The E Indian region behaves in the opposite way, with closed-open occurring closest to shore and closed-closed farthest offshore. A seasonal analysis shows that trajectories that begin as closed cells are more common in the spring in our southern-hemisphere regions, and in summer in the NE Pacific. A seasonal breakdown of the fraction of trajectories that stay closed as opposed to breaking into open or disorganized shows a strong trade-off between closed-closed and closed-disorganized MCC, while the fraction of trajectories that transition to open remains more constant throughout the year. The trade-off between closed-closed and closed-disorganized transitions hints at meteorological forcing driving the closed-disorganized transition. Specifically, the seasonal cycle of closed-closed/closed-disorganized MCC appears synchronized with LTS, which is highest when closed cells tend to remain closed.

A comparison of meteorological and cloud variables as drivers of MCC change shows significantly different conditions associated with closed-disorganized versus closed-open transitions. Transitions to disorganized cells are associated with a stronger diurnal cycle of PBL depth, showing a greater amount of overnight deepening. This is likely driven by the accompanying weaker subsidence, weaker inversion, and drier free troposphere, which allows for enhanced entrainment of dry air into the cloud deck, causing drying and breakup. This contrasts significantly with the closed-open transition, which is associated with reduced N_d, stronger surface winds, and enhanced overnight precipitation in PBLs that begin as meteorologically comparable to the closed-closed set. A cursory analysis suggests that low N_d and heavier overnight rain may independently lead to the closed-open transition. Follow-on analyses are strongly motived to untangle the effects of wind speed, N_d, and rain on the closed-open transition, with the goal of discovering mechanism(s) that drive this transition.

References

Agee, E.M., 1987: Mesoscale cellular convection over the oceans. *Dyn. Atmos. Oceans*, **10**, 317-341.

Bender, F. A.-M., A. Engström, J. Karlsson, 2016: Factors controlling cloud albedo in marine subtropical stratocumulus regions in climate models and satellite observations. *J. Climate,* **29** (10), 3559–3587.

Bennartz, R., 2007: Global assessment of marine boundary layer cloud droplet number concentration from satellites. *J.Geophys. Res*., **112**, D02201, doi:10.1029/2006JD007547.

Boers, R., J. A. Acarreta, and J. L. Gras, 2006: Satellite monitoring of the first indirect aerosol effect: Retrieval of the droplet concentration of water clouds. *J. Geophys. Res*., **111**, D22208, doi:10.1029/2005JD006838.

Bretherton, C. S and M. C. Wyant, 1997: Moisture transport, lower-tropospheric stability, and decoupling of cloud-topped boundary layers. *J. Atmos. Sci.*, **54**(1), 148–167. https://doi.org/10.1175/1520-0469(1997)054<0148:MTLTSA>2.0.CO;2

Bretherton, C. S., R. Wood, R. C. George, D. Leon, G. Allen, and X. Zheng, 2010: Southeast Pacific stratocumulus clouds, precipitation and boundary layer structure sampled along 20 S during VOCALS-Rex. *Atmos. Chem. Phys*., **10**, 639–10 654.

Colon-Robles, M., R. M. Rauber, and J. B. Jensen, 2006: Influence of low level wind speed on droplet spectra near cloud base in trade wind cumulus. *Geophys. Res. Lett*., **33**, L20814, doi:https://doi.org/10.1029/2006GL027487.

Copernicus Climate Change Service (C3S), 2017: ERA5: Fifth generation of ECMWF atmospheric reanalyses of the global climate . Copernicus Climate Change Service Climate Data Store (CDS), Accessed: December, 2019. https://cds.climate.copernicus.eu/cdsapp#!/home

Dee, D. P., and Coauthors, 2011: The ERA-Interim reanalysis: Configuration and performance of the data assimilation system. *Quart. J. Roy. Meteor. Soc*., **137**, 553–597, doi:10.1002/qj.828.

Eastman, R. and R. Wood, 2016: Factors controlling low-cloud evolution over the eastern subtropical oceans: A Lagrangian perspective using the A-Train Satellites. *J. Atmos. Sci.,* **73**, 331-351.

Eastman, R., R. Wood, and C. S. Bretherton, 2016: Time scales of clouds and cloud-controlling variables in subtropical stratocumulus from a Lagrangian perspective. *J. Atmos. Sci.*, **73**, 3079-3091.

Eastman, R., R. Wood, and K. T. O, 2017: The subtropical stratocumulus-topped planetary boundary layer: a climatology and the Lagrangian evolution. *J. Atmos. Sci*., **74**, 2633-2656.

Eastman R., Lebsock, M., and R. Wood, 2019: Warm Rain Rates from AMSR-E 89-GHz Brightness Temperatures Trained Using CloudSat 380 Rain-Rate Observations. *Journal of Atmospheric and Oceanic Technology*, **36**, 1033–1051.

Fu, D., Di Girolamo, L., Liang, L., and G. Zhao, 2019: Regional Biases in MODIS Marine Liquid Water Cloud Drop Effective Radius Deduced Through Fusion With MISR, *J. Geophys. Res.-Atmos*., **124**, 13182–13196, https://doi.org/10.1029/2019JD031063.

Galero, R., and coauthors, 2017: The Modern-Era Retrospective Analysis for Research and Applications, Version 2 (MERRA-2), *J. Climate,* **30** (14), 5419–5454, doi: 10.1175/JCLI-D-16-0758.1

Grosvenor, D. P., & Wood, R., 2018: Daily MODIS (MODerate Imaging Spectroradiometer) derived cloud droplet number concentration global dataset for 2003-2015. *Centre for Environmental Data Analysis*, January, 2020. http://catalogue.ceda.ac.uk/uuid/cf97ccc802d348ec8a3b6f2995dfbbf.

Guichard, F. and F. Couvreux, 2017: A short review of numerical cloud-resolving models, *Tellus A: Dynamic Meteorology and Oceanography*, 69:1, 1373578.

Hahn, C.J., and S.G. Warren, 2007: A gridded climatology of clouds over land (1971-96) and ocean (1954-97) from surface observations worldwide. Numeric Data Package NDP-026E, CDIAC, Department of Energy, Oak Ridge, Tennessee.

Hartmann, D., M. E.Ockert-Bell, and M. L. Michelsen, 1992: The effect of cloud type on Earth's energy balance: Global analysis. *J. Climate*, **5**, 1281–1304.

Hubanks, P. A., M. D. King, S. Platnick, and R. Pincus, 2008: MODIS atmosphere L3 gridded product. NASA Algorithm Theoretical Basis Doc. ATBD-MOD-30, 90 pp.

Kazil, J., G. Feingold, and T. Yamaguchi, 2016: Wind speed response of marine non-precipitating stratocumulus clouds over a diurnal cycle in cloud-system resolving simulations. *Atmos. Chem. Phys.,* **16**, 5811–5839.

King, M. D., and Coauthors, 2003: Cloud and aerosol properties, precipitable water, and profiles of temperature and humidity. IEEE Trans. *Geosci. Remote Sens*., **41**, 442–458, doi:10.1109/TGRS.2002.808226.

Klein, S. A., Hall, A., Norris, J. R., & R. Pincus, 2017: Low-Cloud Feedbacks from Cloud-Controlling Factors: A Review. *Surveys in Geophysics*, **38**(6), 1307-1329. doi:10.1007/s10712-017-9433-3.

L'Ecuyer, T. S., Y. Hang; A. V. Matus; Z. Wang, 2019: Reassessing the Effect of Cloud Type on Earth's Energy Balance in the Age of Active Spaceborne Observations. Part I: Top of Atmosphere and Surface *J. Climate,* **32** (19), 6197–6217.

Lebsock, M. D., and T. S. L'Ecuyer, 2011: The retrieval of warm rain from CloudSat. *J.Geophys. Res.*, **116**, D20209, doi:10.1029/2011JD016076.

Maddux, B. C., S. A. Ackerman, and S. Platnick, 2010: Viewing geometry dependencies in MODIS cloud products. *J. Atmos. Oceanic Technol.,* **27**, 1519–1528, doi:10.1175/ 2010JTECHA1432.1.

McCoy, D. T., F. A. M. Bender, J. K. C., Mohrmann, D. L. Hartmann, R. Wood, and D. P. Grosvenor, 2017: The global aerosol-cloud first indirect effect estimated using MODIS, MERRA and AeroCom, *J. Geophys. Res.-Atmos.,* 1779–1796, https://doi.org/10.1002/2016JD026141.

McCoy, I. L., R. Wood J. K. Fletcher, 2017: Identifying Meteorological Controls on Open and Closed Mesoscale Cellular Convection Associated with Marine Cold Air Outbreaks, *Journal of Geophysical Research: Atmospheres*, **122**, 11, 678–11,702.

Miller, M. A., and S. E. Yuter, 2013: Detection and characterization of heavy drizzle cells within subtropical marine stratocumulus using AMSR-E 89-GHz passive microwave measurements. *Atmos. Meas. Tech*., **6**, 1–13.

Mitrescu, C., T. L'Ecuyer, J. Haynes, S. Miller, and J. Turk, 2010: CloudSat precipitation profiling algorithm: Model description. *J. Appl. Meteor. Climatol.,* **49**, 991–1003, doi:10.1175/2009JAMC2181.1.

Muhlbauer, A., McCoy, I. L., & R. Wood, 2014: Climatology of stratocumulus cloud morphologies: microphysical properties and radiative effects. *Atmospheric Chemistry and Physics,* **14**(13), 6695-6716. doi:10.5194/acp-14-6695-2014.

Norris, J. R. 1998: Low cloud type over the ocean from surface observations. Part I: Relationship to surface meteorology and the vertical distribution of temperature and moisture J. Climate, **11** (3), 369–382.

Oreopoulos, L., 2005: The impact of subsampling on MODIS level-3 statistics of cloud optical thickness and effective radius. *IEEE Trans. Geosci. Remote Sens*., **43**, 366–373, doi:10.1109/TGRS.2004.841247.

Possner, A., R. Eastman, F. Bender, and F. Glassmeier, 2020: Deconvolution of boundary layer depth and aerosol constraints on cloud water path in subtropical stratocumulus decks, *Atmos. Chem. Phys*., **20**, 3609–3621, https://doi.org/10.5194/acp-20-3609-2020.

Qu, X., Hall, A., Klein, S. A., & A. M. DeAngelis, 2015: Positive tropical marine low-cloud cover feedback inferred from cloud-controlling factors. *Geophysical Research Letters*, **42**(18), 7767-7775. doi:10.1002/2015gl065627.

Savic-Jovcic, V., and B. Stevens, 2008: The structure and mesoscale organization of precipitating stratocumulus. *J. Atmos. Sci*., **65**, 1587–1605.

Scott, R. C., Myers, T. A., Norris, J. R., Zelinka, M. D., Klein, S. A., Sun, M, and D. R. Doelling, 2020: Observed Sensitivity of Low-Cloud Radiative Effects to Meteorological Perturbations over the Global Oceans. *J. Climate*, **33** (18): 7717–7734.

Stevens, B., and et al, 2020: Sugar, gravel, fish and flowers: Mesoscale cloud patterns in the trade winds. *Quart. J. Roy. Meteor. Soc.,* **146**, 141–152.

Terai, C. R. and R. Wood, 2013: Aircraft observations of cold pools under marine stratocumulus, *Atmos. Chem. Phys*., **13**, 9899–9914, https://doi.org/10.5194/acp-13-9899-2013.

Vaughan, M., S. Young, D. Winker, K. Powell, A. Omar, Z. Liu, Y. Hu, and C. Hostetler, 2004: Fully automated analysis of space-based lidar data: an overview of the CALIPSO retrieval algorithms and data products. *SPIE Int. Soc. Opt. Eng*., **5575**, 16-30.

Wang H., and G. Feingold, 2009: Modeling mesoscale cellular structure and drizzle in marine stratocumulus. Part I: impact of drizzle on the formation and evolution of open cells. *J Atmos Sci.,* **66**, 3237–3256. https://doi.org/10.1175/2009JAS3022.1

Wentz, F. J. and T. Meissner. 2004: AMSR-E/Aqua L2B Global Swath Ocean Products derived from Wentz Algorithm. Version 2. [L3 LWP]. Boulder, Colorado USA.

Wood, R., 2012: Stratocumulus clouds, *Mon. Weather Rev*., **140**, 2373–2423.

Wood, R., & D. L. Hartmann, 2006: Spatial variability of liquid water path in marine low cloud: The importance of mesoscale cellular convection. *Journal of Climate*, **19**(9), 1748– 1764.

Wood, R., and C. S. Bretherton, 2004: Boundary layer depth, entrainment, and decoupling in the cloud-capped subtropical and tropical marine boundary layer. *J. Climate*, **17**, 3576–3588.

Wood, R., K. K. Comstock, C. S. Bretherton, C. Cornish, J. Tomlinson, D. R. Collins, and C. Fairall, 2008: Open cellular structure in marine stratocumulus sheets, *J. Geophys. Res*., **113**.

Wood, R., O, K.-T., Bretherton, C. S., Mohrmann, J., Albrecht, B. A., Zuidema, P., . . . and P. Minnis, 2018: Ultraclean Layers and Optically Thin Clouds in the Stratocumulus-to-Cumulus Transition. Part I: Observations. *Journal of the Atmospheric Sciences,* **75**(5), 1631-1652. doi:10.1175/jas-d-17-0213.1.

Yuan, T., Song, H., Wood, R., Mohrmann, J., Meyer, K., Oreopoulos, L., and S. Platnick, 2020: Applying deep learning to NASA MODIS data to create a community record of marine low cloud mesoscale morphology, *Atmos. Meas. Tech. Discuss*., in review, https://doi.org/10.5194/amt-2020-61.

Tables

Closed-Closed	Closed-Open	Closed-Disorganized
High LTS	Heavier drizzle at night	Deep PBL
Cool SST	Low Nd	Weak Subsidence
High Nd	Strong Wind Speed	Low LTS
Low Rain Rate		Warm SST
Shallow PBL		Dry Free Troposphere

Table 1. The dominant environmental and cloud variables associated with our three 24-hour MCC transitions.

Figure Captions

Figure 1. Mesoscale Cellular Convection (MCC) classifications overlaid on the corresponding MODIS Aqua image of clouds in the SE Pacific. Classifiers are defined: 0 – open cells, 1 – closed cells, 3 – disorganized cells.

Figure 2. Example frequency distributions of MCC classifiers within a 200km observation radius of each Lagrangian sampling point. Any classification with >50% representation in the distribution is considered the MCC type for that sample.

Figure 3. The mean locations of composited 24-hour trajectories for all three possible MCC transition types within each study region.

Figure 4. The fraction of all available trajectories per 100-day sampling window that start as closed cells, showing a strong yearly cycle of closed cells.

Figure 5. The fraction of trajectories that begin as closed cells per 100-day sampling window that shows a specific transition in MCC classification for each study region.

Figure 6. Composited 24-hour evolution of cloud variables for trajectories that begin as closed, but evolve into open (red) cells, disorganized cells (black), or stay closed (blue). Broken down by study region.

Figure 7. Composited 24-hour evolution of environmental variables for trajectories that begin as closed, but evolve into open (red) cells, disorganized cells (black), or stay closed (blue). Broken down by region.

Figure 8. Composited 24-hour evolution of anomalies of cloud variables for trajectories that begin as closed, but evolve into open (red) cells, disorganized cells (black), or stay closed (blue). Anomalies are calculated by removing the 100-day running mean centered on each day in each 1°x1° grid box for day and night separately.

Figure 9. Composited 24-hour evolution of anomalies of environmental variables for trajectories that begin as closed, but evolve into open (red) cells, disorganized cells (black), or stay closed (blue). Anomalies are calculated by removing the 100-day running mean centered on each day in each 1°x1° grid box for day and night separately.

Figure 10. The 24-hour evolution of N_d composited for our three trajectory sets (blue: closed-closed, red: closed-open, black: closed-disorganized) for three different N_d products: (a) our default product, (b) Grosvenor 2018 N_d from MODIS c5, (c) McCoy et al. (2017) MERRA aerosol regression N_d.

Figure 11. A closer look at composited trajectories showing the 24-hour changes of N_d for sets of trajectories beginning as closed for all trajectories with (a) below-median 0-hour

precipitation probability and (b) above median 0-hour precipitation probability. Precipitation probability is shown for sets of above- and below-median 0-hour N_d (c and d) to show that the overnight precipitation spike associated with closed-open occurs regardless of 0-hour N_d.

Figures

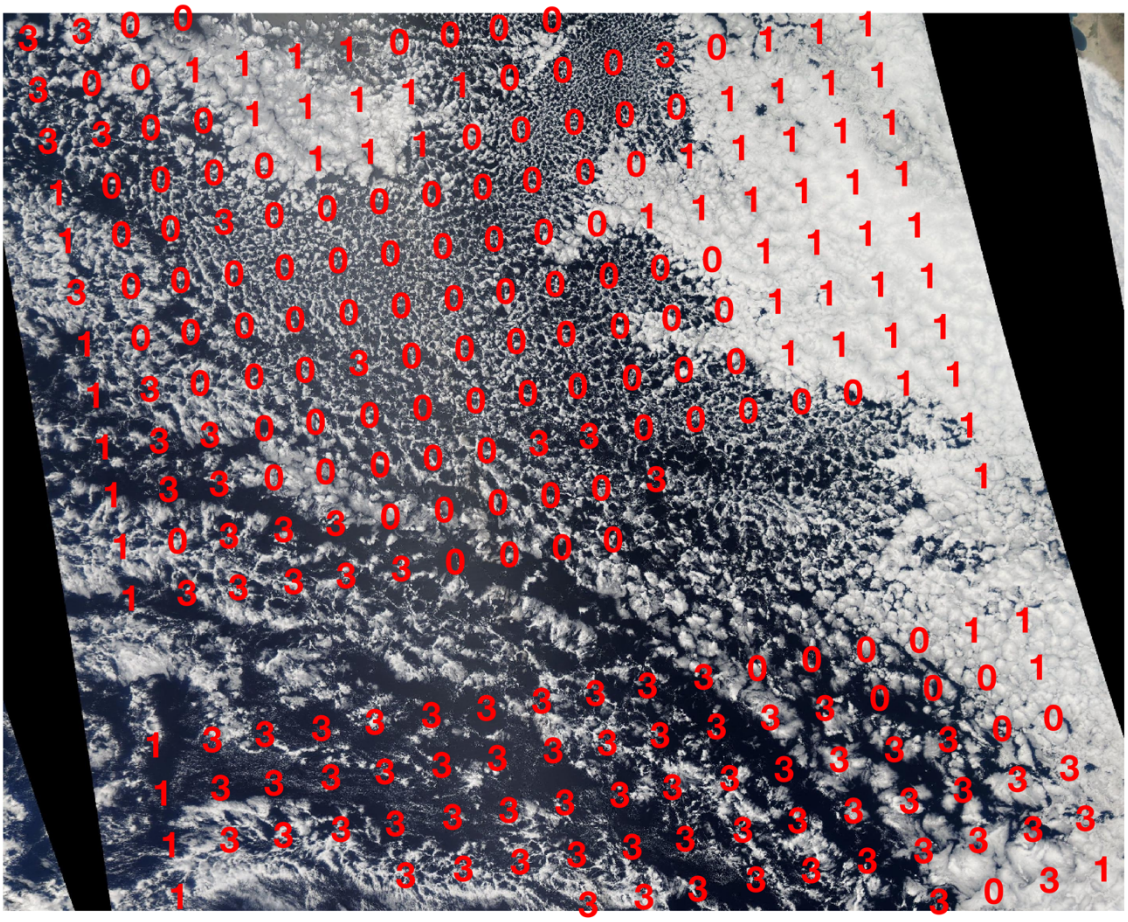

Figure 1. Mesoscale Cellular Convection (MCC) classifications overlaid on the corresponding MODIS Aqua image of clouds in the SE Pacific. Classifiers are defined: 0 – open cells, 1 – closed cells, 3 – disorganized cells.

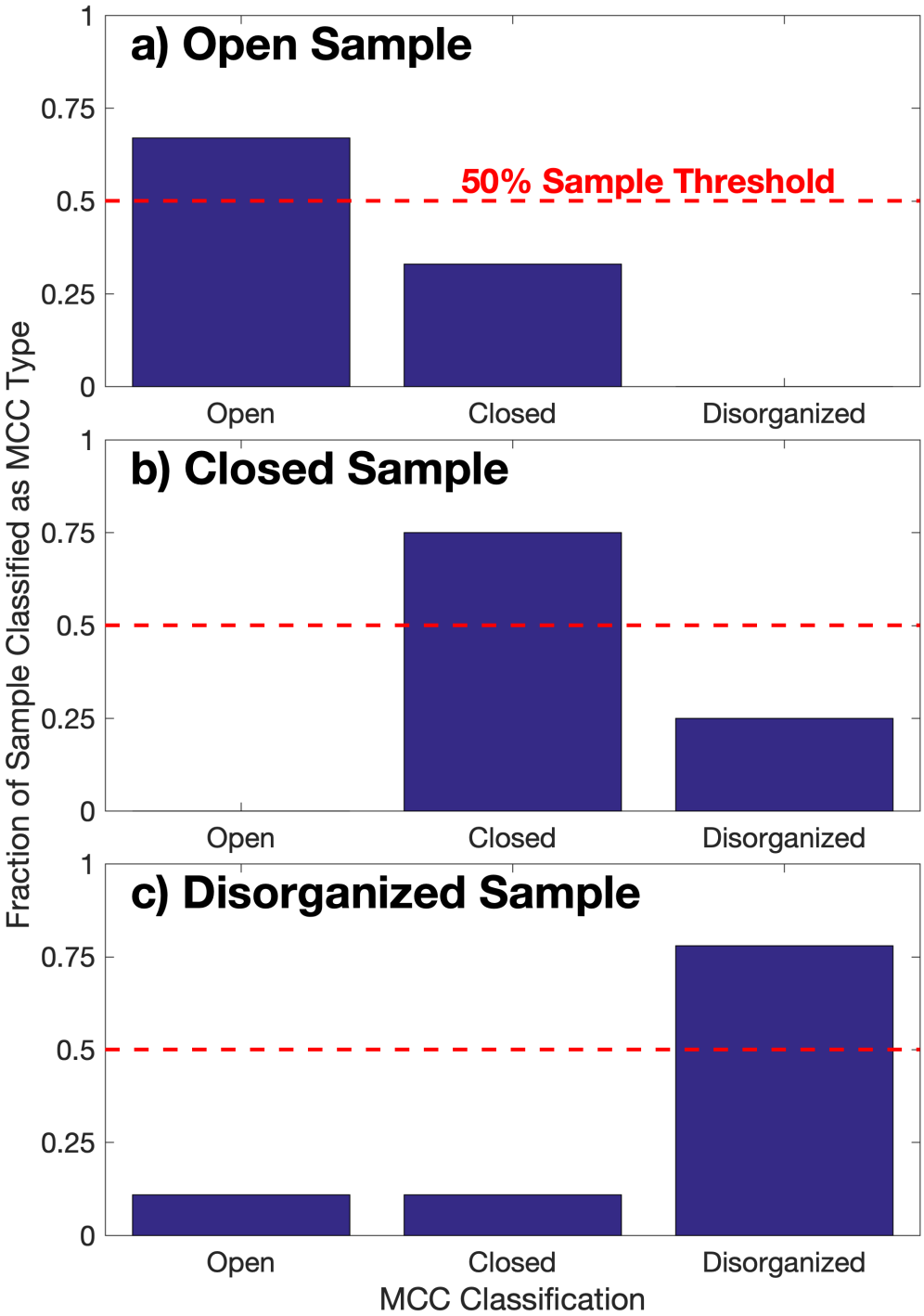

Figure 2. Example frequency distributions of MCC classifiers within a 200km observation radius of each Lagrangian sampling point. Any classification with >50% representation in the distribution is considered the MCC type for that sample.

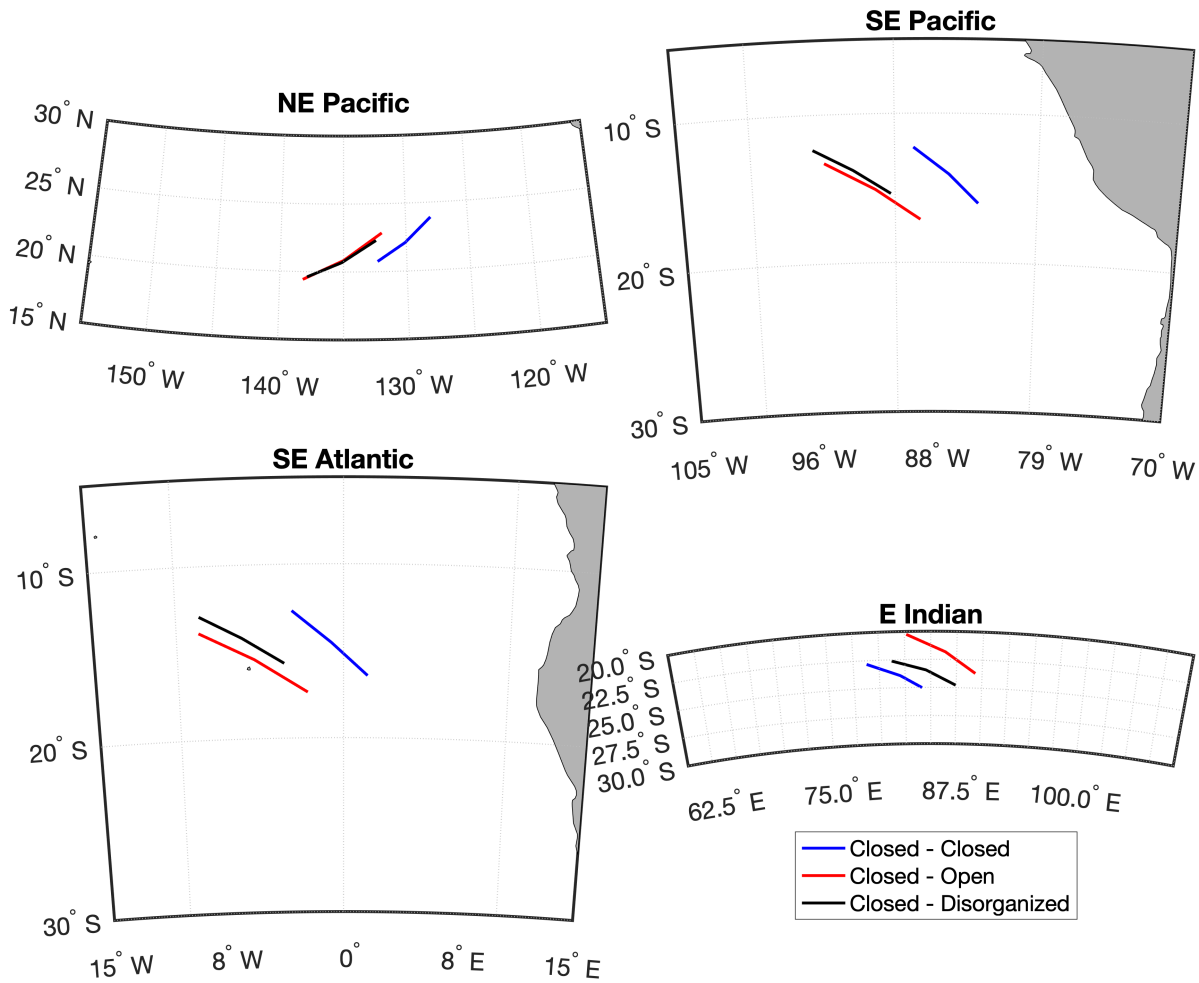

Figure 3. The mean locations of composited 24-hour trajectories for all three possible MCC transition types within each study region.

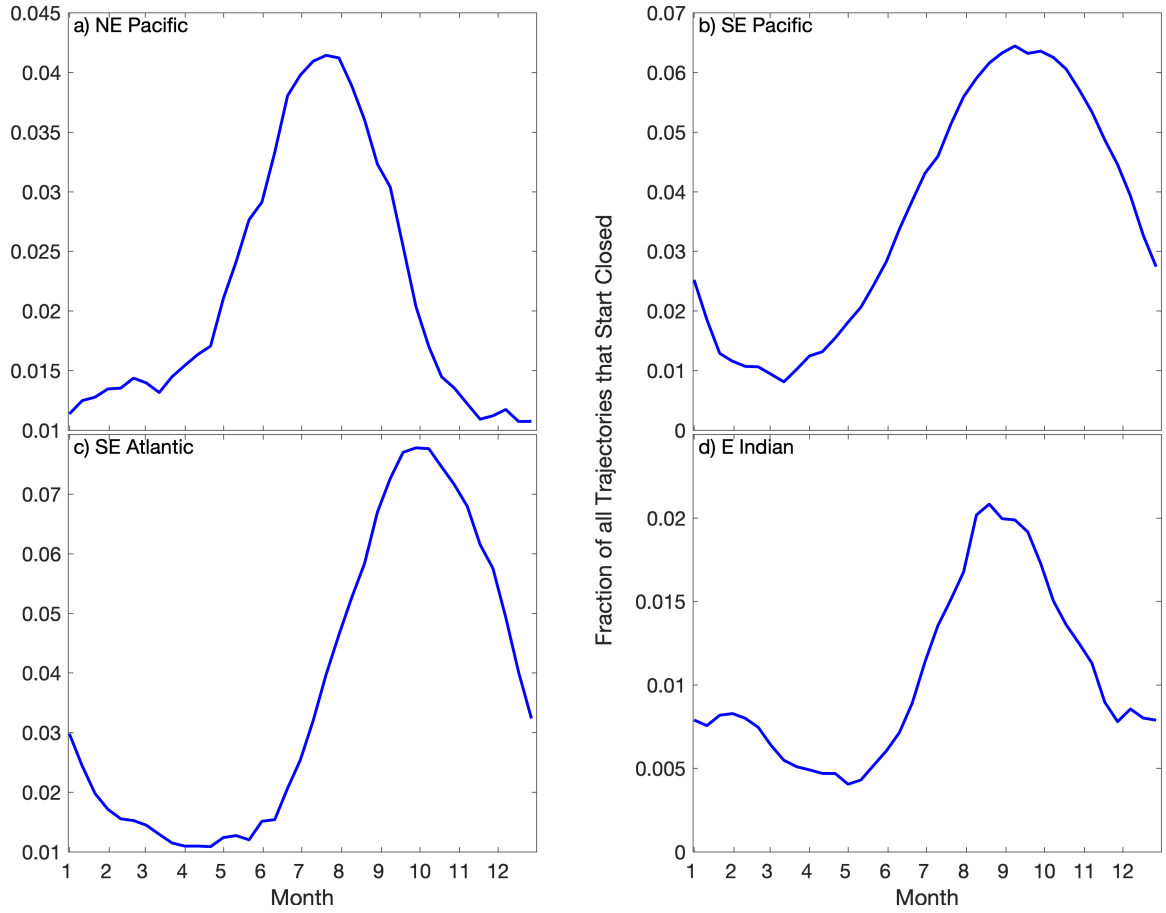

Figure 4. The fraction of all available trajectories per 100-day sampling window that start as closed cells, showing a strong yearly cycle of closed cells.

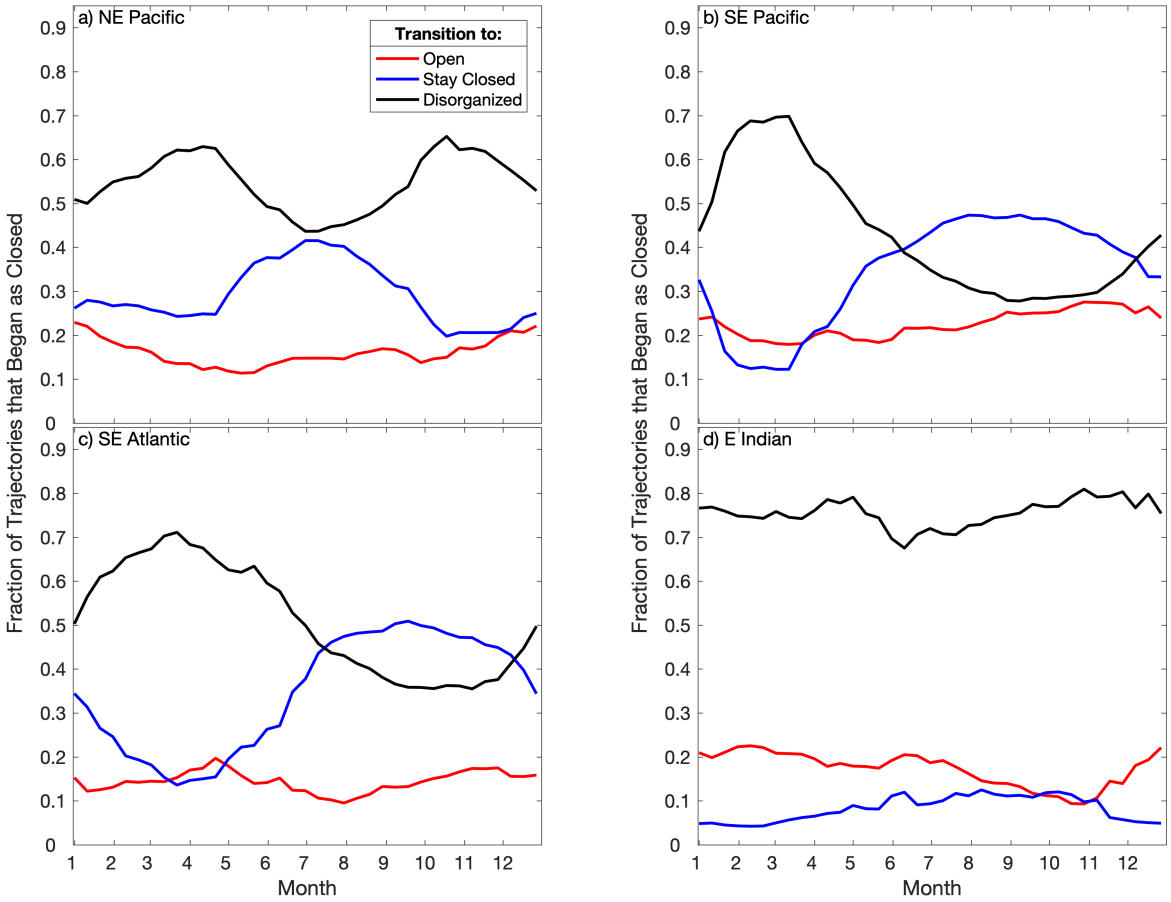

Figure 5. The fraction of trajectories that begin as closed cells per 100-day sampling window that shows a specific transition in MCC classification for each study region.

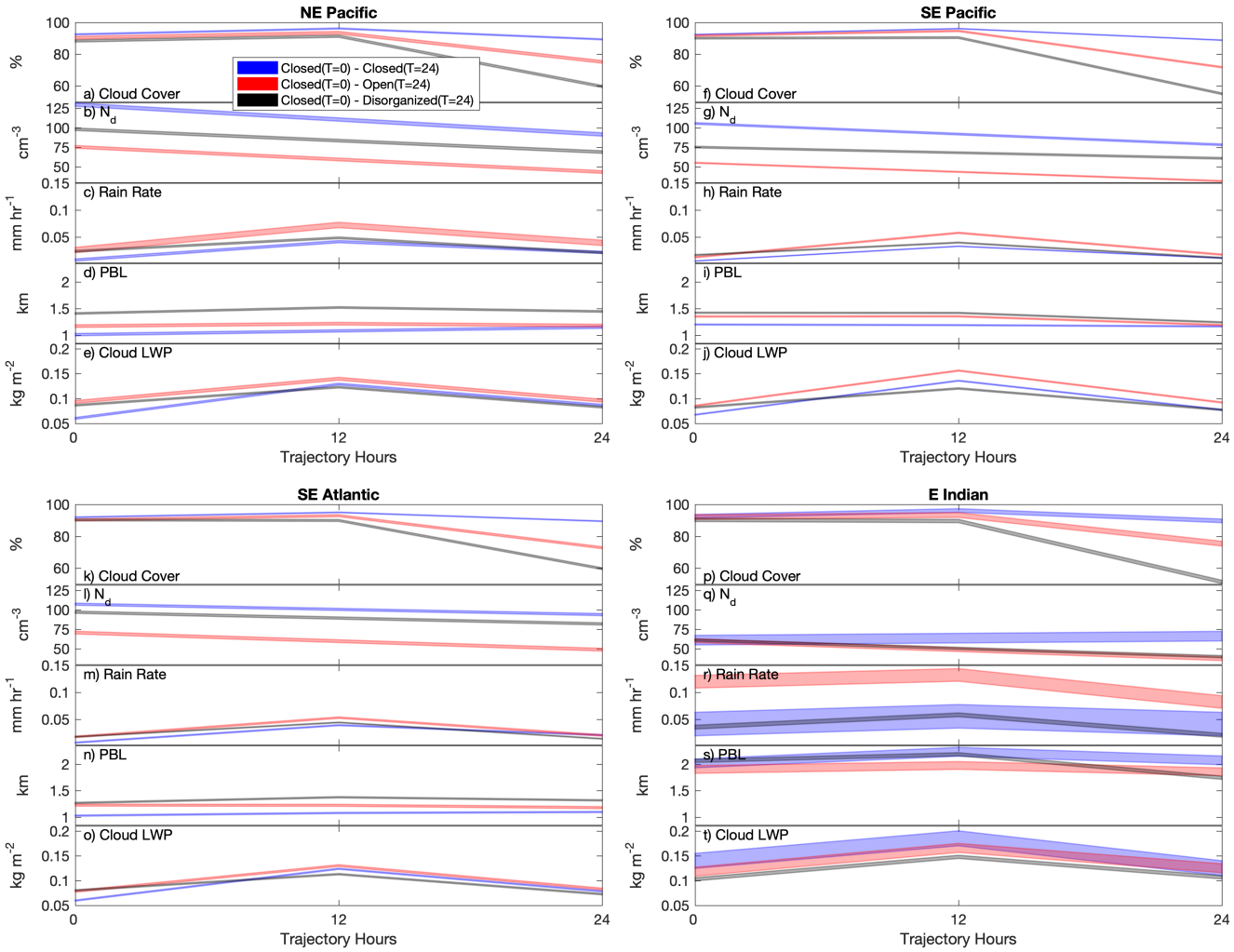

Figure 6. Composited 24-hour evolution of cloud variables for trajectories that begin as closed, but evolve into open (red) cells, disorganized cells (black), or stay closed (blue). Broken down by study region.

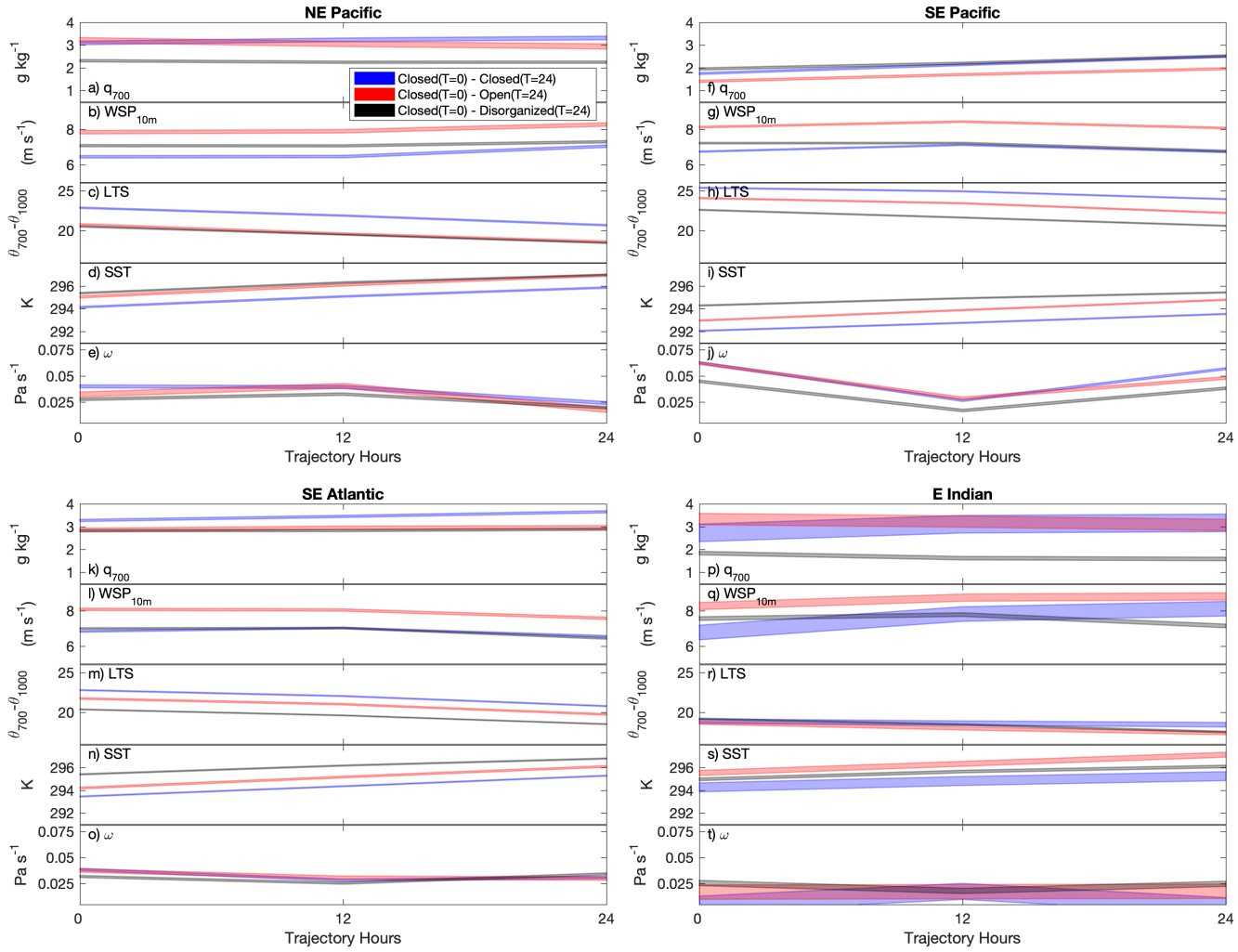

Figure 7. Composited 24-hour evolution of environmental variables for trajectories that begin as closed, but evolve into open (red) cells, disorganized cells (black), or stay closed (blue). Broken down by region.

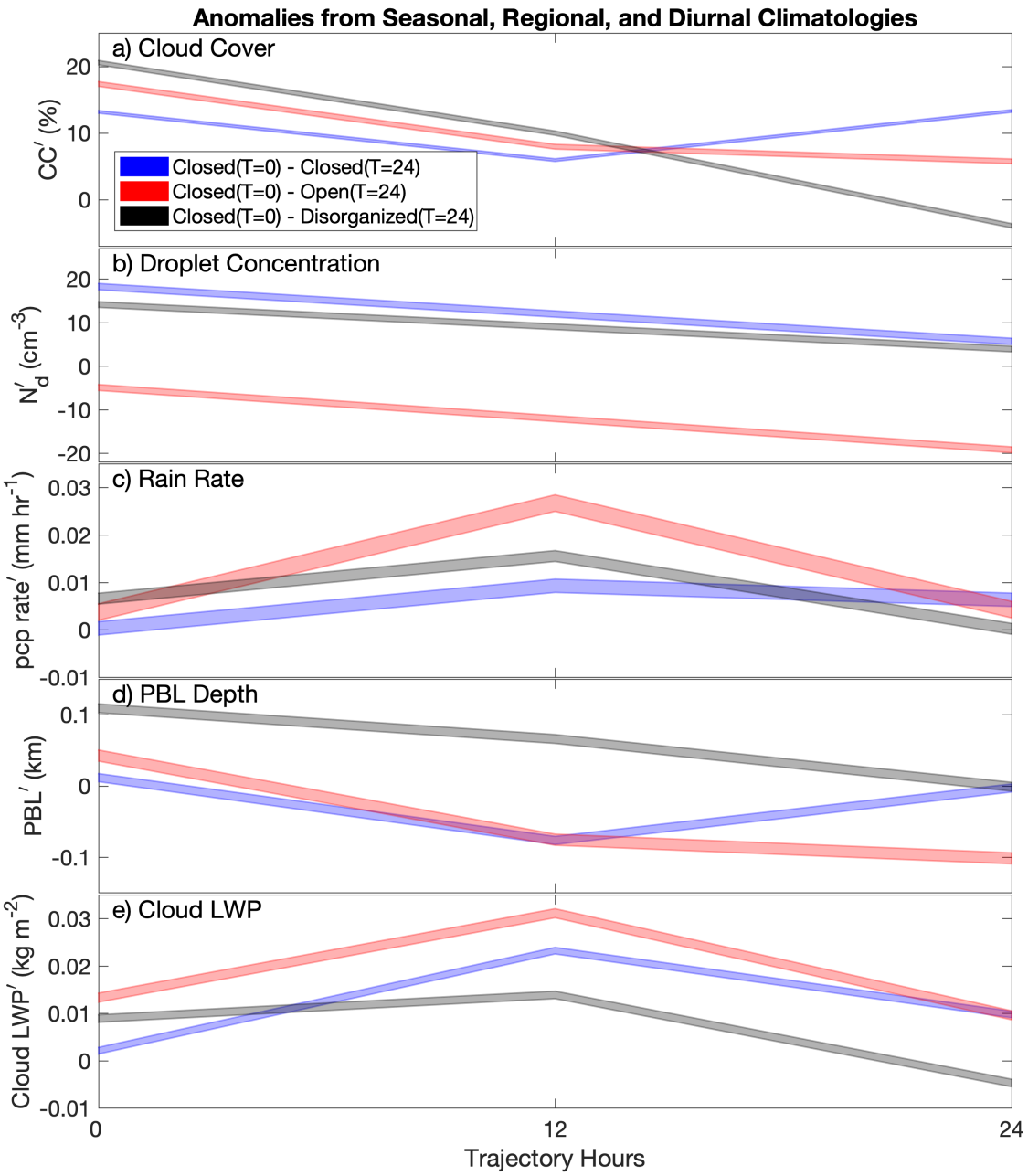

Figure 8. Composited 24-hour evolution of anomalies of cloud variables for trajectories that begin as closed, but evolve into open (red) cells, disorganized cells (black), or stay closed (blue). Anomalies are calculated by removing the 100-day running mean centered on each day in each 1°x1° grid box for day and night separately.

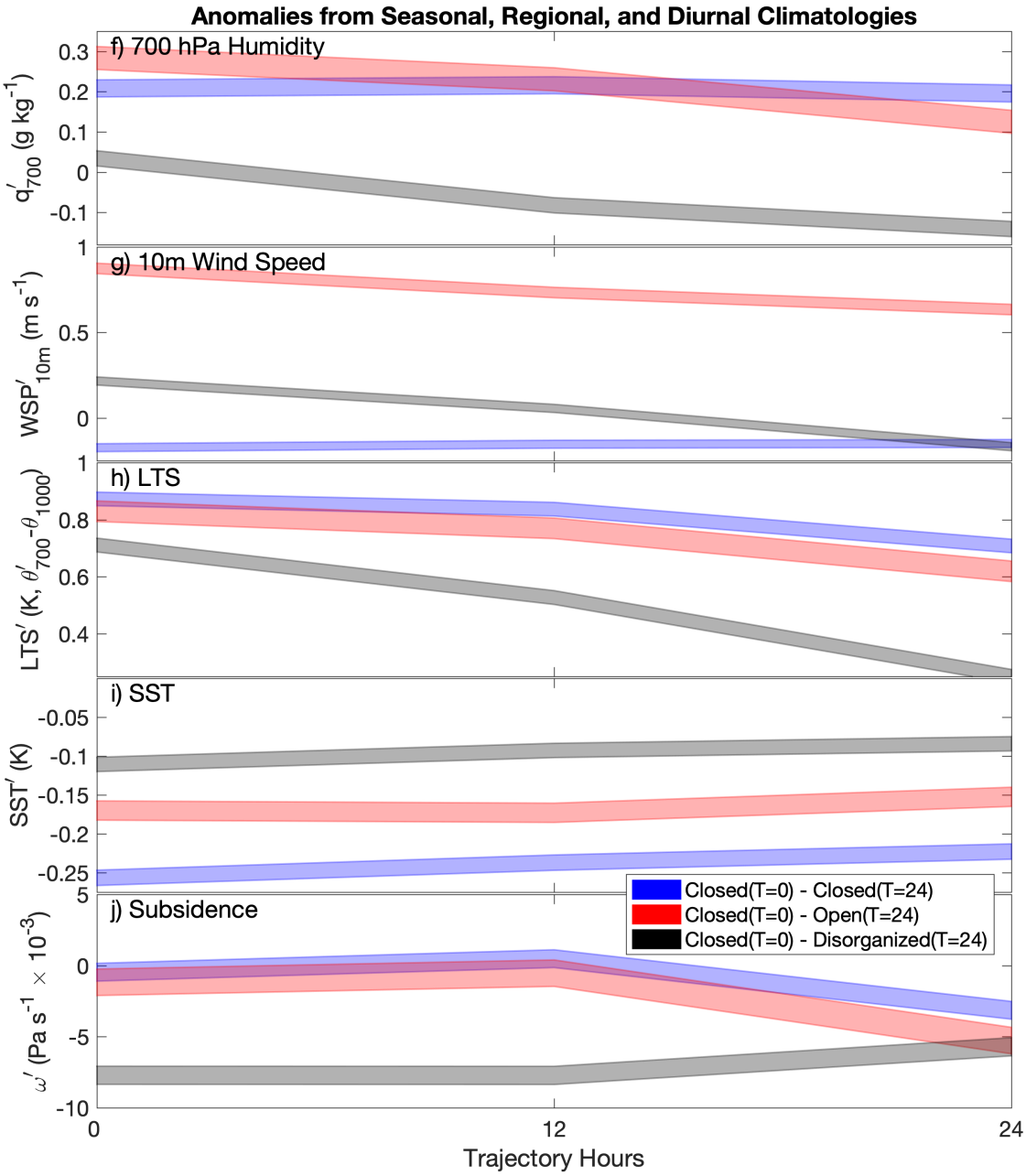

Figure 9. Composited 24-hour evolution of anomalies of environmental variables for trajectories that begin as closed, but evolve into open (red) cells, disorganized cells (black), or stay closed (blue). Anomalies are calculated by removing the 100-day running mean centered on each day in each 1°x1° grid box for day and night separately.

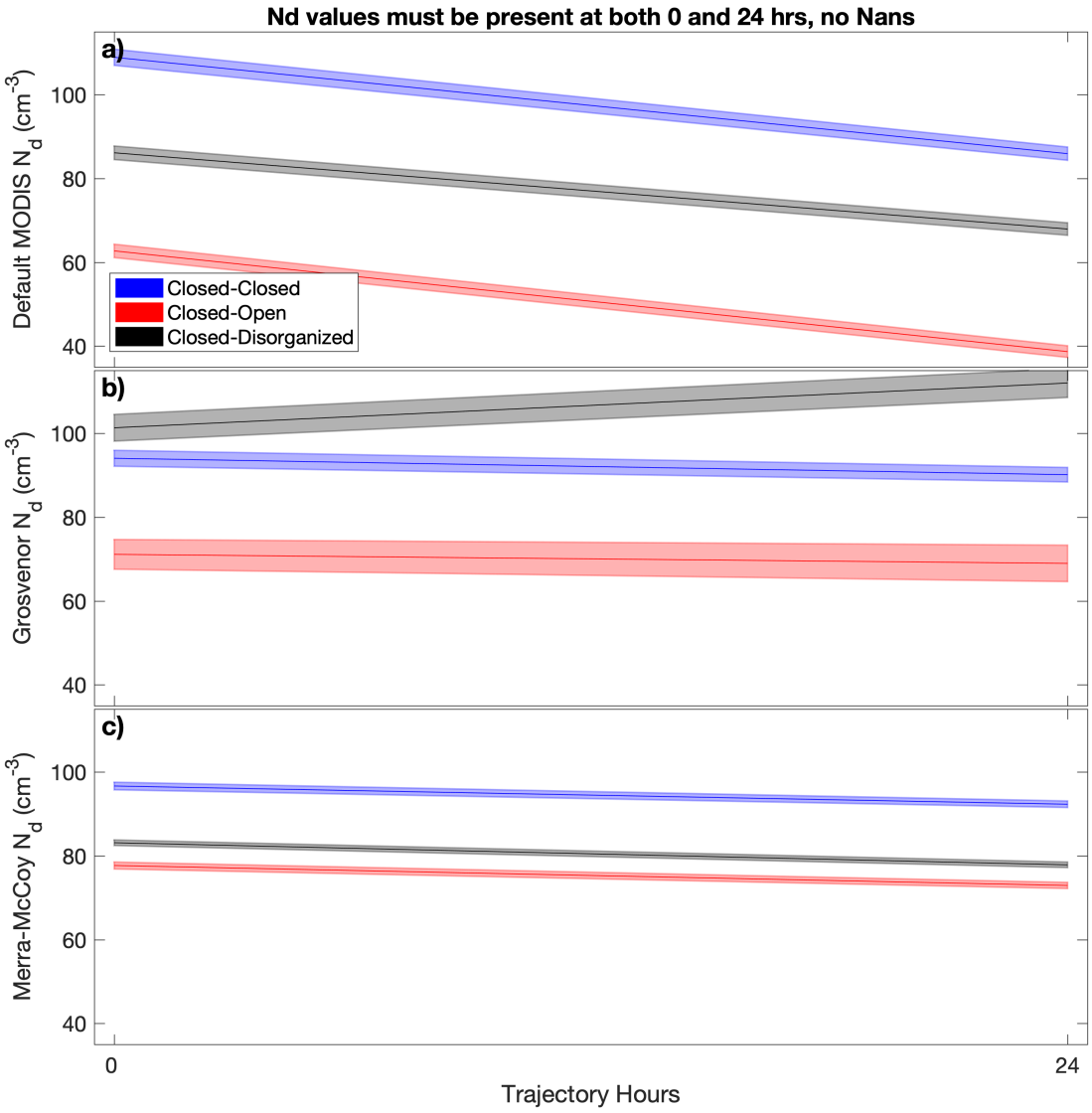

Figure 10. The 24-hour evolution of N_d composited for our three trajectory sets (blue: closed-closed, red: closed-open, black: closed-disorganized) for three different N_d products: (a) our default product, (b) Grosvenor 2018 N_d from MODIS c5, (c) McCoy et al. (2017) MERRA aerosol regression N_d.

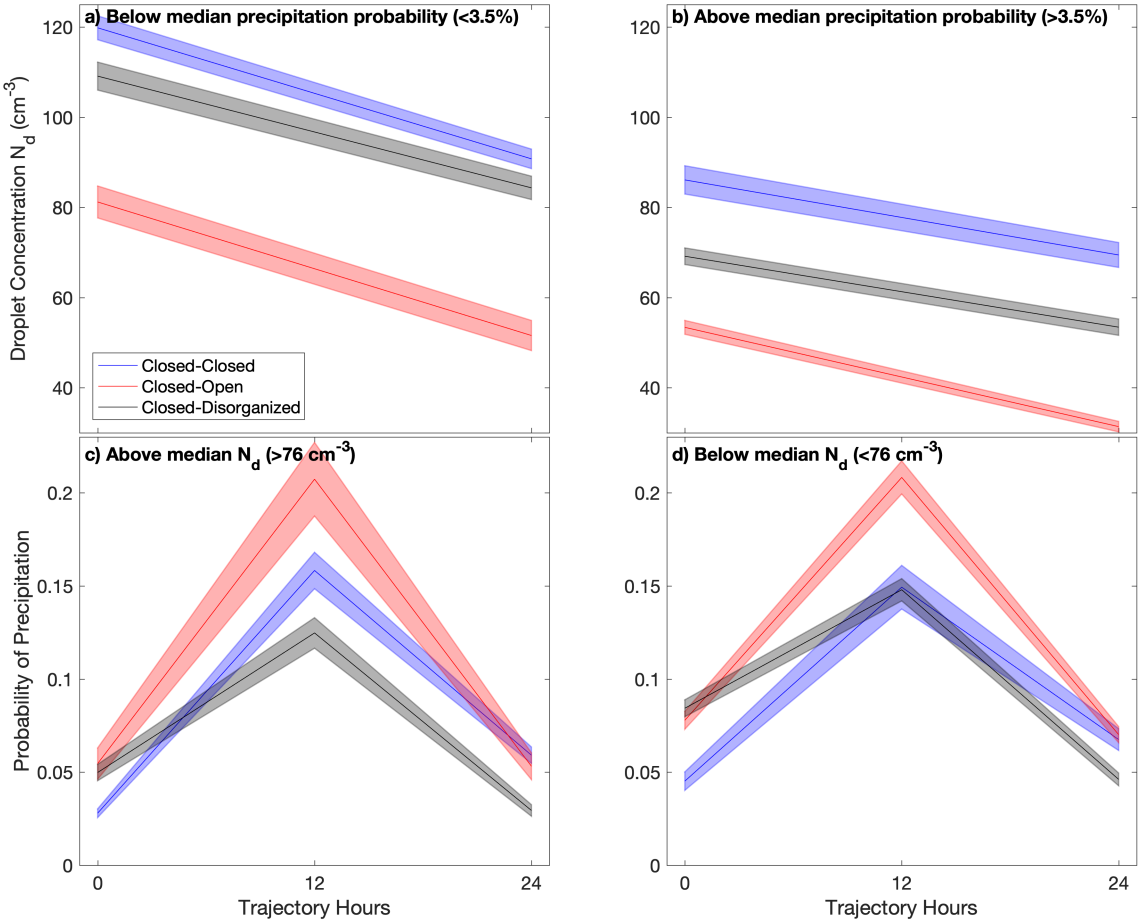

Figure 11. A closer look at composited trajectories showing the 24-hour changes of N_d for sets of trajectories beginning as closed for all trajectories with (a) below-median 0-hour precipitation probability and (b) above median 0-hour precipitation probability. Precipitation probability is shown for sets of above- and below-median 0-hour N_d (c and d) to show that the overnight precipitation spike associated with closed-open occurs regardless of 0-hour N_d.